RHESSI HARD X-RAY IMAGING SPECTROSCOPY OF EXTENDED SOURCES AND THE PHYSICAL PROPERTIES OF ELECTRON ACCELERATION REGIONS IN SOLAR FLARES

Yan Xu,[1] A. Gordon Emslie,[1] and G. J. Hurford[2]

ABSTRACT

In this study we present the results of a new approach to studying the acceleration and propagation of bremsstrahlung-producing electrons in solar flares. The method involves an analysis of the size of extended solar flare structures as a function of photon energy. Hard X-ray images from 10 M-class limb events, observed by the *Reuven Ramaty High Energy Solar Spectroscopic Imager* (*RHESSI*) to have the general form of a single extended source, were analyzed by forward fitting to the source visibilities in each energy band. On average the source sizes σ increased slowly with photon energy ϵ as $\sigma \sim \epsilon^{1/2}$. This behavior is consistent neither with the predictions of a single-loop thermal model nor with a model in which nonthermal electrons are injected into a constant-density structure from a compact acceleration region. While a nonuniform density distribution along the flare loop can in principle reconcile the data with a nonthermal collisional model with point-source injection, the resulting density profiles are highly questionable. On the other hand, the data *are* consistent with a nonthermal collisional model that incorporates an *extended* acceleration region, perhaps in combination with a localized thermal source. We present best-fit results on the density and length of this acceleration region. To our knowledge, this is the first quantitative empirical analysis of the physical characteristics of electron acceleration regions in solar flares.

Subject headings: Sun: activity — Sun: flares — Sun: X-rays, gamma rays

1. INTRODUCTION

The characteristics of energetic electrons accelerated during solar flares can be investigated through study of the hard X-ray bremsstrahlung that they produce upon scattering off ambient ions (see, e.g., Tandberg-Hanssen & Emslie 1988). With the successful launch of the *Reuven Ramaty High Energy Solar Spectroscopic Imager* (*RHESSI*; Lin et al. 2002), we have entered an era of hard X-ray imaging spectroscopy in which photon spectra and, hence, the spectra of the bremsstrahlung-emitting electrons can, in principle, be inferred at different locations throughout the source. This not only provides clues as to the location of the acceleration region but also allows an *empirical* study of the physics of electron transport within the source.

In this paper we present the results from a new method to parametrically investigate electron energy loss processes during flares. The method utilizes parametric forward fitting of source images in different energy bands to study the *global*, rather than local, dependence of the hard X-ray emission (i.e., the spatial properties as a function of energy rather than the energy dependence as a function of position). It also employs newly developed techniques to determine (and fit) the source visibilities (i.e., two-dimensional spatial Fourier components) in each energy band, with the added benefit that statistical uncertainties in the recovered parameters (and so in the inferred source properties) can be determined.

In § 2 we discuss the selection of events analyzed in this paper. In § 3 we describe the details of the fitting procedure used. In § 4 we present theoretical predictions on the variation of source size with photon energy ϵ, and we compare these model predictions with observations in § 5. In § 6 we discuss the significance of the results obtained.

2. EVENT SELECTION

For the proposed study of source size with energy, it is clearly appropriate to use sources that have an "extended" geometry, rather than, say, a set of isolated high-density footpoints for which the information of interest may occur on size scales below instrumental resolution. Also, to minimize projection effects in the transformation from source to extent on the plane of the sky, we selected events observed "side-on" near the solar limb, i.e., with a heliocentric angle $\theta > 50°$. (An additional event [2002 April 12], closer to disk center but with a well-defined loop geometry, was also included, since it occurred in the same active region as one of the other nine.) This criterion excludes only 35% of the disk, so including flares nearer disk center would not add an appreciable number of events to our sample. We also required that the peak count rate be sufficiently high to permit reliable calculation of source visibilities, yet sufficiently low that pulse pileup effects are unlikely to be significant. As a result, our analysis was restricted to *Geostationary Operational Environmental Satellite* (*GOES*) M-class events, for which the peak count rate ranged from 1000 to 6000 counts s^{-1} per detector.

Of the 370 M-class limb flares observed during the period from 2002 April to 2005 August, 10 events (listed in Table 1) exhibited a well-defined extended-source geometry in CLEAN images (which present an unbiased perspective on the source morphology); for such events, a fit to a single curved elliptical source is therefore a reasonable procedure. In Figure 1, we present both clean images (*first and third rows*) and curved elliptical fitted maps (*second and fourth rows*) of each flare in two different energy channels.

3. DATA REDUCTION

RHESSI provides spatial information by using a set of nine rotating modulation collimators (RMCs) to time-modulate the detected flux so that imaging information is encoded in observed rapid time variations of the detected counts (Hurford et al. 2002). Recently an alternative approach to the data analysis has been

[1] Department of Physics, Oklahoma State University, Stillwater, OK 74078; yan.xu@okstate.edu, gordon.emslie@okstate.edu.
[2] Space Sciences Laboratory, University of California at Berkeley, 7 Gauss Way, Berkeley, CA 94720-7450; ghurford@ssl.berkeley.edu.

TABLE 1
LIST OF EVENTS

Date	Integration Time	Location on Solar Disk (Heliocentric [West, North]; arcsec)	*GOES* Classification
2002 Apr 12...........	17:33:56–17:34:56	414, 443	M4.5
2002 Apr 15...........	00:05:00–00:10:00	784, 382	M4.1
2002 Apr 17...........	17:00:00–17:05:00	928, −247	M1.1
2003 Jun 17	22:47:00–22:50:00	−813, −147	M6.8
2003 Jul 10	14:15:00–14:19:00	943, 220	M3.7
2003 Dec 2	22:54:00–22:58:00	917, −340	M1.5
2004 May 21.........	23:47:00–23:50:00	−757, −157	M2.6
2004 Aug 31.........	05:33:00–05:38:00	944, 96	M1.4
2005 Jun 1	02:37:00–02:41:00	−692, −294	M1.8
2005 Aug 23	14:27:00–14:31:00	920, −236	M3.0

introduced (G. J. Hurford et al. 2008, in preparation) that interprets the observed time variations directly in terms of a set of visibilities (calibrated measurements of specific spatial Fourier components of the source distribution). As with image reconstruction in radio interferometry, the set of X-ray visibilities can then be used to infer the spatial properties of the X-ray source. In this case we use a forward-fit algorithm that fits the observed visibilities to simple parametric source forms. The variation of the forward-fit parameters with photon energy provides the information necessary for our study.

Since the fundamental geometry in the events studied is that of an extended, curved source, we chose to fit curved elliptical Gaussian source forms. Such forms are described by the equation

$$I(x,y;\epsilon) = I_0 \exp(-s^2/2\sigma^2) \exp(-t^2/2\tau^2), \quad (1)$$

where $s(x,y)$ is a coordinate along a circular arc of radius ρ, t is the coordinate locally perpendicular to this arc, and $\sigma(\epsilon)$ and $\tau(\epsilon)$ are the standard deviations of the source extent in the parallel and perpendicular directions, respectively. The source geometry (eq. [1]) is characterized by a set of seven parameters: the location (x_0, y_0) of the center of the arc on which the source lies, the radius of curvature of the arc ρ, the direction θ defining the direction on the plane of the sky between the center of the arc and the emission centroid, the peak intensity I_0, and the standard

deviations[3] σ and τ. Corresponding to the image form (eq. [1]) are the visibilities

$$V(u,v;\epsilon) = \int_{-\infty}^{\infty} \int_{-\infty}^{\infty} I(x,y;\epsilon) \exp[2\pi i(ux+vy)] \, dx \, dy, \quad (2)$$

characterized by the same seven parameters $(x_0, y_0, \rho, \theta, I_0, \sigma, \tau)$. Forward fitting the data with such parametric visibility forms yields the best-fit values for each of the parameters involved.

It is important to note that this visibility-based forward-fit technique provides not only the values of the seven parameters defining the source geometry [and in particular the longitudinal source extent $\sigma(\epsilon)$] *but also the quantitative uncertainties associated with counting statistics.*

4. MODEL PREDICTIONS

Before presenting the results of the parametric fits, we first consider a few simple models for the variation of source size with energy. The first model (§ 4.1) consists of a thermal source located near the apex of the loop. We then turn our attention to

---

[3] The forward-fit software actually provides the full widths at half-maximum s_{FWHM}, t_{FWHM}, which are readily converted to σ and τ using the relationships $\{s,t\}_{\mathrm{FWHM}} = (8 \ln 2)^{1/2} \{\sigma, \tau\}$.
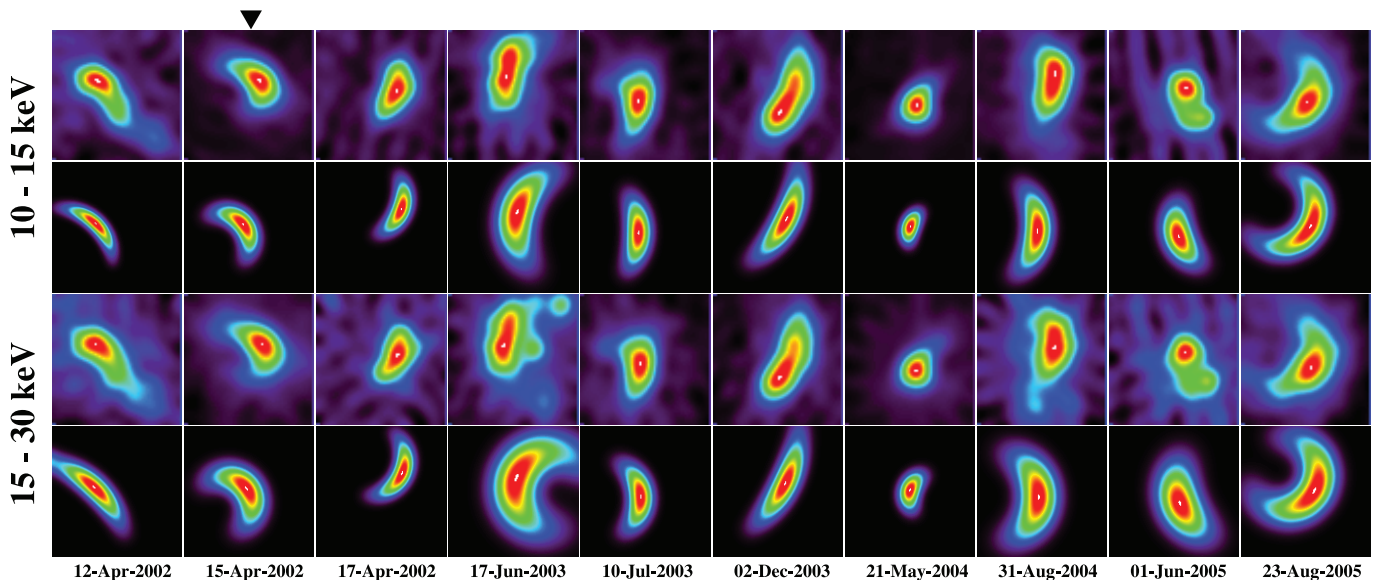

FIG. 1.—CLEAN and visibility-based forward-fit images for all the events listed in Table 1. *First and third rows:* *RHESSI* hard X-ray CLEAN images in the energy ranges 10–15 and 15–30 keV. *Second and fourth rows:* Visibility-based curved elliptical Gaussian fits for the same energy ranges.
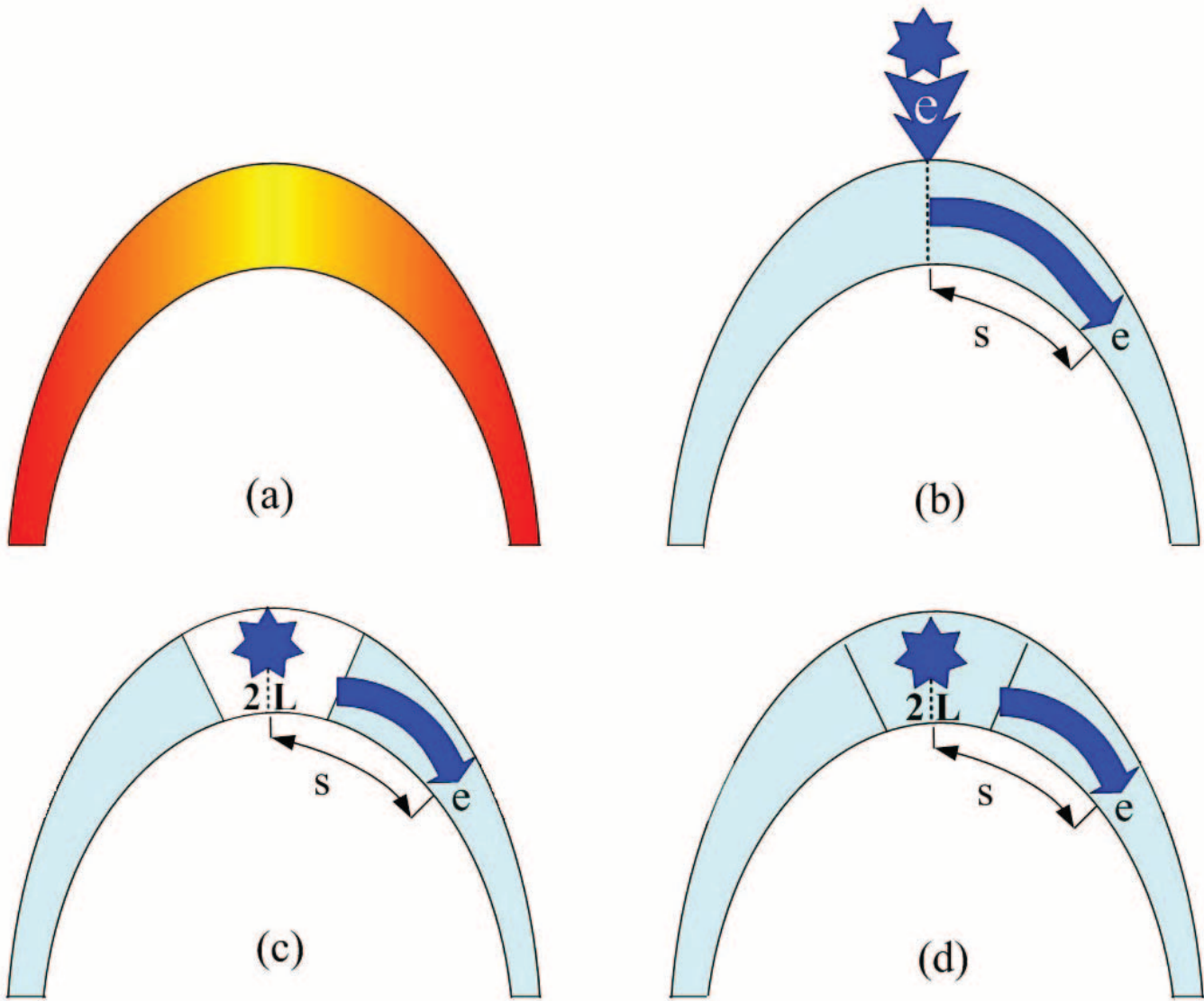
FIG. 2.—Source models: (a) thermal model; (b) collisional model with a compact acceleration region; (c) collisional model with an extended (*tenuous*) acceleration region of half-length L; (d) collisional model with an extended (*dense*) acceleration region.

models involving the injection and propagation of nonthermal electrons. In § 4.2.1, we consider a model in which electrons are injected from a compact acceleration region into a uniform-density collisional target. We also consider (§ 4.2.2) a modification of this simple model incorporating an electron energy loss rate that varies with energy according to a formula that is a generalization of the Coulomb collision energy loss rate. In § 4.2.3 we briefly discuss point injection collisional models that have a nonuniform density in the target. We then make a rather important modification to the model by including an acceleration region of finite length, both tenuous (§ 4.2.4) and dense (§ 4.2.5).

4.1. Thermal Model

We first consider (Fig. 2a) an extended-source thermal model, with the temperature T varying with position s along the loop according to

$$T(s) = T_0 \exp \frac{-s^2}{2\sigma_T^2}. \qquad (3)$$

The thermal bremsstrahlung emission at position s obeys the proportionality

$$I(\epsilon, s) \sim \frac{1}{\epsilon [T(s)]^{1/2}} e^{-\epsilon/kT(s)}, \qquad (4)$$

i.e.,

$$I(\epsilon, s) \sim \frac{1}{\epsilon T_0^{1/2}} \exp \frac{s^2}{4\sigma_T^2} \exp \left(-\frac{\epsilon}{kT_0} \exp \frac{s^2}{2\sigma_T^2} \right). \qquad (5)$$

The intensity at position s relative to the (maximum) intensity at $s = 0$ is then given by

$$j(\epsilon, s) \equiv \frac{I(\epsilon, s)}{I(\epsilon, 0)} = \exp \frac{s^2}{4\sigma_T^2} \exp \left[-\frac{\epsilon}{kT_0} \left(\exp \frac{s^2}{2\sigma_T^2} - 1 \right) \right]. \qquad (6)$$

Let us now define the "size" of the source by the position of the point s^* at which $\ln j(\epsilon, s^*)$ is equal to $-\phi^2$ [i.e., $j(\epsilon, s)$ is a fraction $e^{-\phi^2}$ of the peak intensity]:

$$\frac{s^{*2}}{4\sigma_T^2} - \frac{\epsilon}{kT_0}\left(\exp\frac{s^{*2}}{2\sigma_T^2} - 1\right) = -\phi^2. \quad (7)$$

Given (T_0, σ_T), this equation can be solved numerically for $s^*(\epsilon, \phi)$. It is instructive, however, to investigate the solution in certain limits. For sources with modest temperature variation over their length ($s^{*2} \ll \sigma_T^2$) we obtain

$$\frac{s^{*2}}{2\sigma_T^2}\left(\frac{1}{2} - \frac{\epsilon}{kT_0}\right) = -\phi^2. \quad (8)$$

Temperatures found from thermal analysis of hard X-ray flare spectra are typically of the order of a few keV, much less than the energy range under observation. Applying, then, the further simplification $\epsilon \gg kT_0$, equation (8) reduces to

$$s^{*2} = \frac{2\sigma_T^2 kT_0}{\epsilon}\phi^2, \quad (9)$$

i.e.,

$$s^* = \sqrt{2kT_0}\,\phi\,\frac{\sigma_T}{\epsilon^{1/2}}. \quad (10)$$

The source "size"[4] s^* therefore scales as σ_T, as expected, but also as $(kT_0/\epsilon)^{1/2}$. We have found empirically that the logarithmic slope

$$\zeta = \frac{d\ln\sigma}{d\ln\epsilon} \equiv \frac{d\ln s^*}{d\ln\epsilon} = -\frac{1}{2} \quad (11)$$

obtained with the above approximations in fact agrees very well with the exact (numerical) solution of equation (7) over a rather wide range of ϵ. However, a more important point, one that holds for more general forms of temperature distribution $T(s)$, is that *any simple thermal model with a peak temperature at its centroid will be characterized by a decrease in source size with energy*, a prediction that is readily testable through observation.

4.2. Nonthermal Models

The basic assumption of all nonthermal models considered here is that electrons are injected from an acceleration region into the coronal portion of a magnetic loop. We choose to consider only scenarios in which the coronal portion of the loop is sufficiently dense to cause substantial modification to the electrons as they propagate through it, so that most of the electrons are stopped in the coronal portion of the loop (Veronig & Brown 2004). There is therefore negligible footpoint emission in such a model; most of the emission is spread over the coronal source, so this model does *not* apply to those flares that do exhibit well-defined footpoint emission.

4.2.1. Point-Source Injection Collisional Model

We assume that the electrons [with a power-law spectrum $F_0(E_0) \sim E_0^{-\delta}$] are injected at the point $s = 0$ (e.g., from an acceleration region exterior to the main loop; see Fig. 2b) and

lose their energy through Coulomb collisions. Such a scenario would be appropriate to, for example, the "standard model" with a compact acceleration region (Hirayama 1974; Kopp & Pneuman 1976; Forbes & Malherbe 1986; Somov & Kosugi 1997; Lin & Forbes 2000), in which the electrons are accelerated by shocks in a region above the loop apex and injected into the loop body through an inverted Y-type trajectory. For such a model, we follow the analysis of Brown et al. (2002), who showed that the hard X-ray intensity as a function of position s (cm) can be written as

$$I(\epsilon, s) = \Gamma n(s)\frac{1}{\epsilon}\int_\epsilon^\infty \frac{dE}{[E^2 + 2KN(s)]^{(\delta+1)/2}}, \quad (12)$$

where $N(s)$ is the column density $\int_0^s n(s)\,ds$ at the point s, $n(s)$ is the local number density (cm^{-3}), and K and Γ are constants. From this equation, we can derive the (intensity-weighted) mean source column density $\overline{N}(\epsilon)$:

$$\overline{N}(\epsilon) = \frac{\int_0^\infty N(s)I(\epsilon,s)\,ds}{\int_0^\infty I(\epsilon,s)\,ds} = \left(\frac{\epsilon^2}{K}\right)\frac{\delta-2}{(\delta-3)(\delta-4)}, \quad (13)$$

where we have used $dN = n(s)\,ds$. The essential result of equation (13) is that $\overline{N}(\epsilon) \sim \epsilon^2$, viz., that images at large photon energies should have one-sided centroids farther away from the original acceleration region. This result is consistent with the parallel analysis of Brown et al. (2002) and physically results from the fact that the penetration column depth of an electron scales as the square of the electron energy. Of course, we cannot observe the column density $\overline{N}(\epsilon)$ directly, but rather the longitudinal standard deviation σ (eq. [1]). In a source of constant density n, inserting the Gaussian form (1) for $I(\epsilon, s)$ shows that σ and $\overline{N}$ are simply related: $\sigma = (\pi/2)^{1/2}(\overline{N}/n)$; we consider the nonuniform density case in § 4.2.3 below. A key result, however, is that, in contrast to the thermal source considered in § 4.1, *the size of the source should increase with energy*, no matter what the density structure. For collisional energy losses in a uniform target, the quantitative prediction is that

$$\zeta = \frac{d\ln\sigma}{d\ln\epsilon} \equiv \frac{d\ln\overline{N}}{d\ln\epsilon} = 2. \quad (14)$$

4.2.2. Point-Source Injection Model with Generalized Energy Losses

Here the geometry is still that of Figure 2b, except that we extend the analysis of Brown et al. (2002) by considering (see Emslie et al. 2001) a parametric generalization of the Coulomb collision energy loss formula:

$$\frac{dE}{dN} = -\frac{KE_*^{\alpha-1}}{E^\alpha}, \quad (15)$$

where E_* is a reference energy and α is a constant. This allows us to model a range of physical processes. For Coulomb collisions, $\alpha = 1$. For ohmic losses associated with the driving of a beam-neutralizing return current (e.g., Emslie 1980), the energy loss rate is independent of energy ($\alpha = 0$). Haydock et al. (2001) have studied the modification of the electron spectrum due to the action of wave-particle instabilities driven by the preferential depletion of low-energy electrons by Coulomb collisions (Emslie & Smith 1984). They concluded that the effective energy loss rate was given by $\alpha = \beta/2 - 1$, where β is a "flattening parameter" associated with the formation of plateaus in the electron phase-space distribution function.[5]

---

[4] Although the source "size" s^* is defined somewhat differently than the standard deviation σ (eq. [1]), the two definitions differ by only a multiplicative constant so that the value of the logarithmic slope ζ (eq. [11]) is unaffected by this distinction.

[5] The flattening parameter β is denoted by α in the paper of Haydock et al.

Use of the generalized energy loss formula (15) in turn leads to a generalized expression for the variation of hard X-ray intensity with position in the source (cf. eq. [12]):

$$I(\epsilon, s) = \Gamma n(s) \frac{1}{\epsilon} \int_\epsilon^\infty \frac{E_*^{\alpha-1} \, dE}{\left[E^{\alpha+1} + (\alpha+1)KE_*^{\alpha-1}N\right]^{(\delta+\alpha)/(\alpha+1)}}, \quad (16)$$

and so to a generalization of $\overline{N}(\epsilon)$ as

$$\overline{N}(\epsilon; \alpha) = \left(\frac{\epsilon^{\alpha+1}}{KE_*^{\alpha-1}}\right) \frac{\delta-2}{(\delta-\alpha-2)(\delta-\alpha-3)}. \quad (17)$$

In general, for such an energy loss model the logarithmic slope $\zeta \equiv d \ln \overline{N}/d \ln \epsilon = 1 + \alpha$; setting $\alpha = 1$ (Coulomb collisions) leads us back to equation (13), and, for a uniform density target, $\zeta = 2$ so that once again the size increases with energy.

4.2.3. Point-Source Injection Collisional Model with Nonuniform Target Density

Here the source geometry is again that of Figure 2*b*. However, following Brown et al. (2002) we allow for a nonuniform density $n(s)$ in the target. Through this generalization, the standard Coulomb collisional energy loss model of § 4.2.1 can be made to fit *any* observation in which the source size increases monotonically with photon energy: we simply compare the measured values of $\sigma(\epsilon)$ with the theoretical values of $\overline{N}(\epsilon)$ (eq. [13]) and determine the required density distribution $n(s)$ through the relation $n(s) = n[\sigma(\epsilon)] = \Delta\overline{N}(\epsilon)/\Delta\sigma(\epsilon)$.

4.2.4. Collisional Model with an Extended (Tenuous) Acceleration Region

This scenario (see Fig. 2*c*) is somewhat artificial but, as we shall see, quite instructive. The electrons are accelerated within a region of very low density extending from $s = -L$ to $s = L$ and are injected into a dense external region with uniform density. Straightforwardly, this simply adds a length L to the source size σ found in § 4.2.1, viz. (see eq. [13]),

$$\sigma(\epsilon) = L + \left(\frac{\epsilon^2}{Kn}\right) \frac{\delta-2}{(\delta-3)(\delta-4)}. \quad (18)$$

This is of the form $\sigma = L + bn^{-1}\epsilon^2$, where b is a constant. The value of the logarithmic slope $\zeta \equiv d \ln \sigma/d \ln \epsilon$ for such a source model varies from $\zeta = 0$ at low energies $\epsilon \ll (KnL)^{1/2}$ (reflecting the fact that the electrons stop in a very short distance after leaving the acceleration region, so that the [fixed length] acceleration region is the dominant component of the overall source extent) to $\zeta = 2$ at high energies $\epsilon \gg (KnL)^{1/2}$ (for which the extent of the acceleration region is negligible compared to the collisional stopping distance and so the point-source injection model, with $\sigma \sim \epsilon^2$, is a reasonable approximation). This model clearly fails to account for the type of source structures studied here, since it predicts a "gap" in the emission from $s = -L$ to $s = L$). However, it nevertheless semiquantitatively demonstrates the effect of incorporating a finite acceleration region length and may well be appropriate for analyses of flares exhibiting a "double footpoint" structure. In the next subsection we develop the notion of a finite acceleration region more physically.

4.2.5. Collisional Model with an Extended (Dense) Acceleration Region

This model (see Fig. 2*d*) is a more physical generalization of the basic model. The electrons are again accelerated in a region
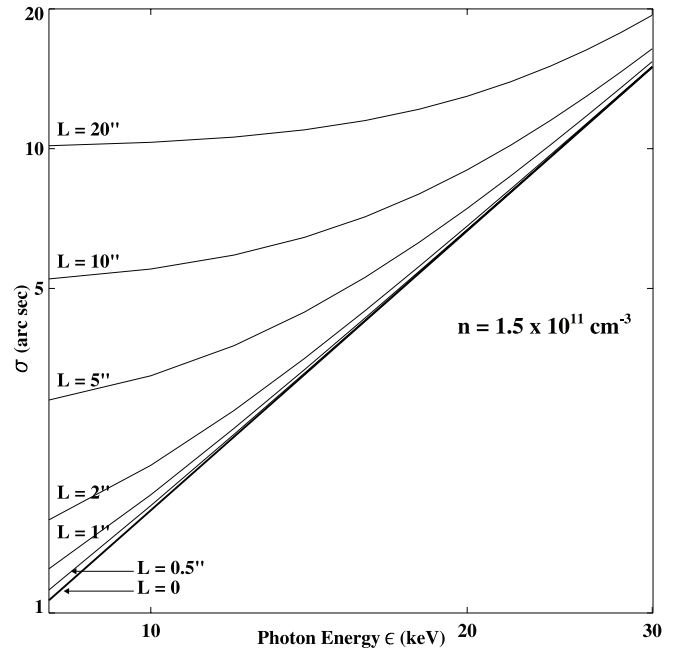

Fig. 3.—Predicted behavior of $\sigma(\epsilon)$ for the collisional model with an extended, dense, acceleration region. Results are shown for a density $n = 1.5 \times 10^{11}$ cm^{-3} and a variety of values of L.

extending from $s_0 = -L$ to $s_0 = L$; however, we now consider this region to have a (uniform) density n equal to that in the rest of the loop. In this case, we can generalize equation (12) to allow both for a continuum of acceleration regions extending from $s_0 = -L$ to $s_0 = L$ and for the fact that electrons propagate in *both* directions toward locations with $|s| \leq L$, so that the injection energy corresponding to an electron of energy E arriving at location s is given by $E_0 = (E^2 + 2Kn|s - s_0|)^{1/2}$. Equation (12) then generalizes to the form

$$I(\epsilon, s) = \Gamma n \frac{1}{2L\epsilon} \int_{-L}^{L} ds_0 \int_\epsilon^\infty \frac{dE}{(E^2 + 2Kn|s - s_0|)^{(\delta+1)/2}}, \quad (19)$$

$$\sigma(\epsilon) = \frac{\int_0^\infty s I(\epsilon, s) \, ds}{\int_0^\infty I(\epsilon, s) \, ds}$$
$$= \frac{\int_0^\infty s \, ds \int_{-L}^{L} ds_0 \int_\epsilon^\infty (E^2 + 2Kn|s - s_0|)^{-(\delta+1)/2} \, dE}{\int_0^\infty ds \int_{-L}^{L} ds_0 \int_\epsilon^\infty (E^2 + 2Kn|s - s_0|)^{-(\delta+1)/2} \, dE}. \quad (20)$$

For a compact acceleration region, $L = 0$, and we recover equation (13).

Equation (20) was evaluated numerically, with results illustrated in Figure 3. At high electron energies E, the acceleration region is collisionally thin and has little effect on the spectrum of electrons emerging from it; the dependence of source size on photon energy ϵ reflects the form of the collisional energy loss function and again scales as ϵ^2. On the other hand, for low values of E, the acceleration region is collisionally thick. Furthermore, since each point within the acceleration region has the same properties, the electron (and photon) spectra are relatively constant throughout it, and hence the source size at low values of the photon energy ϵ (for which low-energy electrons do most of the emitting) is almost *independent* of ϵ. The general behavior of $\sigma(\epsilon)$ is thus a gradual transition from a relatively flat profile ($\zeta = 0$) at low energies to a profile with $\zeta \simeq 2$ at high energies. This behavior is qualitatively similar to the $\sigma \sim L + bn^{-1}\epsilon^2$
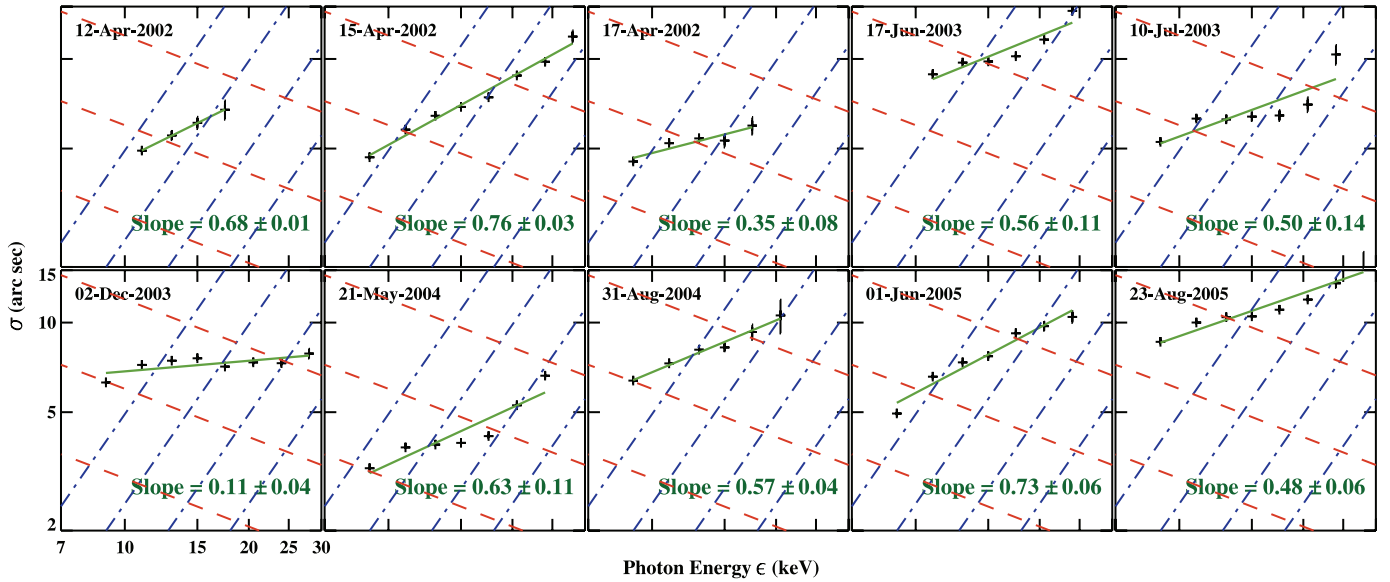
Fig. 4.—Variation of source size σ with photon energy ϵ, superimposed with the predictions of the single-source thermal model (*red descending lines*; slope -0.5; for $T_0 = 10^8$ K and $\sigma_T = 3''$, $6''$, and $12''$ from bottom to top) and the point-source injection collisional model (*blue ascending lines*; slope 2; for loop densities $n = (0.5, 1, 2, 4) \times 10^{11}$ cm^{-3} from left to right).

behavior in the (artificial) tenuous acceleration model of the previous subsection. Thus, if this simple analytic form proves to be a reasonable fit to the data, this provides the impetus to attempt a fit to the more complicated, but more physically correct, expression (20).

5. COMPARISON OF OBSERVATIONS WITH MODEL PREDICTIONS

The visibility-based forward-fitting technique was applied to each of the selected events to determine the energy dependence of $\sigma(\epsilon)$ in each case. The images were produced using the front detectors for RMCs 3, 4, 5, 6, 7, 8, and 9. Data from RMC 1 were not used because its fine resolution ($2.3''$) overresolved the sources; RMC 2 was excluded because it was not segmented early in the mission and so had rather poor energy resolution for these events (Smith et al. 2002).

Up to seven energy channels were used for some events. For some weaker events data is only presented for the moderate-energy channels, because of (1) the low count number in the higher energy channels and (2) very low counts in the lowest energy channel (8–10 keV), which significantly aliased the fits. In order to provide the best count statistics, we chose time intervals of the order of 3–5 minutes, except for the impulsive event on 2002 April 12, for which data were available for only $\sim$1 minute (the error bars on the fit parameters for this event are correspondingly larger).

As a check on the appropriateness of the method, we examined the behavior of the parameters x_0, y_0, ρ, and θ with photon energy. In all cases, these values were virtually independent of energy [for example, for the 2002 April 15 event, the range of locations (x_0, y_0), radii ρ, and orientations θ were $1''$, $1''$, and $1°$, respectively]. The constancy of these values with energy validates not only the assumed source geometry but also the analysis approach.

The second column of Figure 1 (marked with an arrow on top) shows CLEAN images (*first and third rows*) and curved elliptical fits for the same energy channels (*second and fourth rows*) for the event of 2002 April 15 (00:05:00–00:10:00 UT), in the energy[6]

ranges 10–15 and 15–30 keV, respectively. It is apparent that the longitudinal extent[7] of the source is greater at the higher photon energy. Figure 4 shows the observed variation of the longitudinal size σ with energy ϵ (in the log-log domain), together with the best-fit power-law index ζ ($\sigma \sim \epsilon^\zeta$) for each of the events analyzed. Also shown are the theoretical predictions $\sigma(\epsilon)$ of both the simple thermal (§ 4.1) and (point-source injection) collisional models (§ 4.2.1), which are characterized by the temperature peak and standard deviation (T_0, σ_T), and the (uniform) source density n, respectively.[8] The predicted values of ζ are -0.5 and 2, respectively. The slopes of the best-fit lines through the $\sigma(\epsilon)$ points range from $\zeta = 0.11 \pm 0.04$ to 0.76 ± 0.03. None of them is consistent with either the thermal model ($\zeta = -0.5$) or the point-source injection nonthermal model ($\zeta = 2$). A histogram of all results (Fig. 5) makes this point even clearer; the mean value of ζ is about 0.6 ± 0.14, totally inconsistent with the predictions of both these simple models.

This average best-fit value $\zeta \sim \frac{1}{2}$ does correspond to a non-collisional energy loss process with $\alpha = \zeta - 1 \sim -\frac{1}{2}$ (eq. [17]). The only case considered in that section that permits such a value of α is the wave-particle energy redistribution model of Haydock et al. (2001), with "flattening parameter" $\beta = 2(1 + \alpha) \sim 1$. However, close scrutiny of the phase-space distribution curves of Haydock et al. (2001; e.g., their Fig. 3) shows that such a value of β (their α) is not really appropriate to the evolution of the distribution function under wave-particle redistribution

---

[6] In this paper, the energy ranges refer to the directly observed count spectrum, which, at these energies, differs only slightly from the photon spectrum.

[7] It should be noted that *both* the longitudinal length σ and width τ of the sources increase with photon energy ϵ. At this point, we are unable to offer a plausible reason for the latter variation. We also wish to note that an explanation for the behavior of $\tau(\epsilon)$ is substantially outside the scope of the present work, the emphasis of which is on an examination of the behavior of the *longitudinal* extent of the source with energy ϵ and comparison of observed behaviors with the (quite varied) model predictions for this quantity. It is, however, hoped to address possible reasons for the variation of longitudinal source extent τ with photon energy ϵ in a follow-up study.

[8] For the nonthermal model, the predicted behavior also depends slightly on the spectral index δ (see eq. [13]). While it is tempting to use a value of δ given from the source-integrated hard X-ray spectral index γ by the usual thick-target relation $\delta = \gamma + 1$, such a relation is based on a presupposed (collisional) form of energy loss. However, use of a different value of δ changes only the value of the source density n determined by the method and does not affect the principal conclusion of the paper. We have therefore used a value $\delta = 6$ throughout.
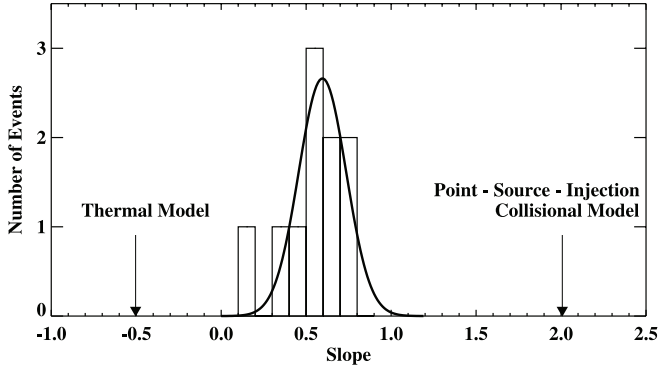
Fig. 5.—Histogram of the best-fit slopes $\zeta \equiv d \ln \sigma(\epsilon)/d \ln \epsilon$ for the 10 events analyzed. A Gaussian fit to the distribution (mean 0.60; standard deviation 0.14) is also shown. The arrows show the predictions of the thermal model and the point-source injection collisional model.

processes (only for values $\beta \sim 6$ does a significant plateau in the phase-space distribution result).

Figure 6 shows, for each event, the density structure $n(s)$ required to obtain the observed behavior of σ from the simple, point-injection, collisional model (see § 4.2.3 and eq. [13]). Qualitatively, a high density causes a rapid change in electron spectrum with distance, and thus a small distance between source centroids at specified energies, so a region of shallow slope ζ corresponds to a high value of $n(s)$. The density profiles generated show significant variations that, while not entirely unacceptable, are at variance with the results of hydrodynamic simulations of flare-heated coronae (e.g., Mariska et al. 1989), which show a relatively uniform structure for the density profile in the corona, especially after an elapsed time period of a few minutes, corresponding to the observations reported here.

Although neither simple model adequately accounts for the data, it is tempting to suggest that, since the observed values of $\zeta \sim 0.6 \pm 0.1$ lie between the respective model predictions of -0.5 and 2, perhaps a *combination* of these two simple models can account for the data. To investigate this more quantitatively, we now consider a "hybrid" model in which the observed emission will be a combination of thermal emission (which we expect to dominate at low energies) and nonthermal emission (which we

expect to dominate at high energies). Since an analysis using a forward fit to a Gaussian determines the source size through measurement of the second moment of the intensity distribution (cf. eq. [1]), the source size of such a hybrid model will in general be given by summing the second moments of the individual sources:

$$
\begin{aligned}
\sigma^2(\epsilon) = & [1 - R(\epsilon)]\sigma^2_{\text{th}}(\epsilon) + R(\epsilon)\sigma^2_{\text{nonth}}(\epsilon) \\
& + R(\epsilon)[1 - R(\epsilon)]D^2(\epsilon).
\end{aligned}
\tag{21}
$$

Here $R(\epsilon)$ is the ratio of the nonthermal hard X-ray flux to the total hard X-ray flux at photon energy ϵ, obtained by fitting the *spatially integrated* spectrum with a sum of thermal and nonthermal components (see, e.g., Holman et al. 2003) and determining the ratio $R(\epsilon) = I_{\text{nonth}}(\epsilon)/[I_{\text{th}}(\epsilon) + I_{\text{nonth}}(\epsilon)]$ as a function of ϵ. We make no assumptions regarding the form of $\sigma_{\text{nonth}}(\epsilon)$; however, following the discussion of § 4.1 leading to equation (10), we represent the thermal source size by $\sigma_{\text{th}}(\epsilon) = A\epsilon^{-1/2}$, where A is a constant proportional to σ_T, the width (in temperature space; see eq. [3]) of the thermal component of the source. Here $D(\epsilon)$ is the separation of the centroids of the thermal and nonthermal source components. This quantity is determined by the relative locations of the low- and high-energy sources and, in practice, is inferred independently from the phase difference in the visibilities at low and high photon energies. In practice $D(\epsilon)$ is very small ($\lesssim 1''$), but it is included here for completeness.

We can now "remove" the contributions of both the thermal component and the separation D of the thermal and nonthermal source centroids to the overall second moment σ^2 (eq. [21]). There remains from this procedure an empirical form for the nonthermal source size

$$
\sigma_{\text{nonth}}(\epsilon) = \sqrt{\frac{\sigma^2(\epsilon) - R(\epsilon)[1 - R(\epsilon)]D^2(\epsilon) - [1 - R(\epsilon)]A\epsilon^{-1}}{R(\epsilon)}},
\tag{22}
$$

which can be compared to the analytic forms considered in § 4.2.

The fit to the observed data $\sigma(\epsilon)$ now involves three parameters: L and n for the nonthermal component and A (or, equivalently, σ_T) for the thermal component. The results of the fits to
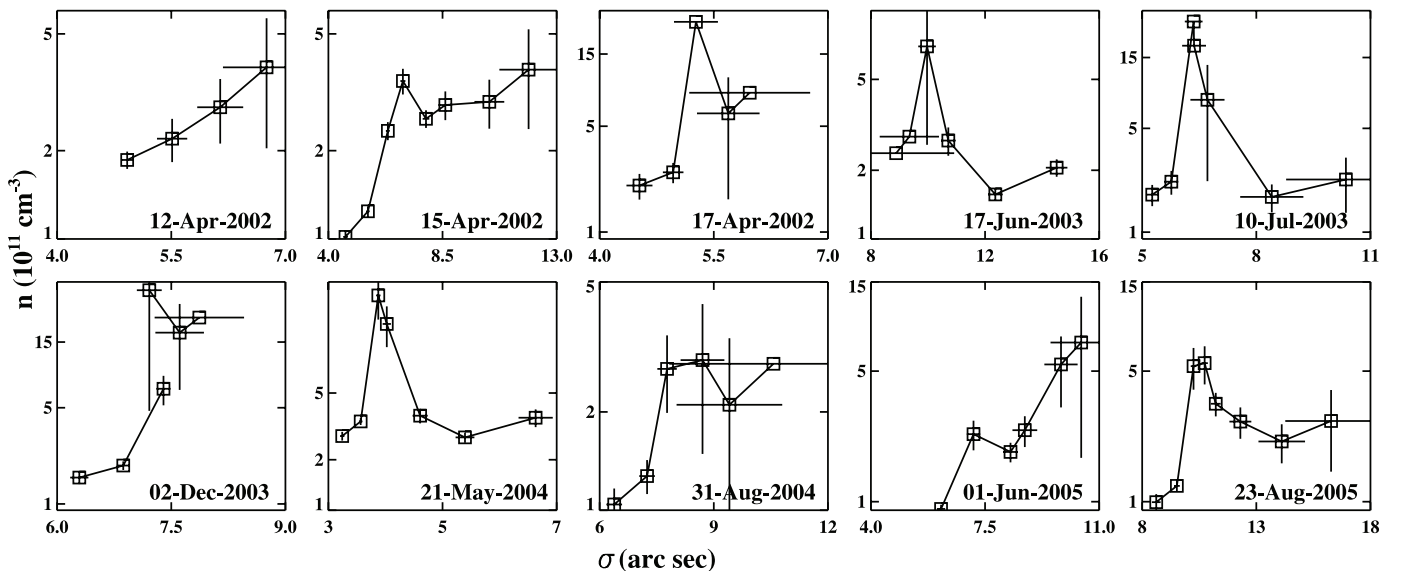

Fig. 6.—Source density profiles $n(s)$ required to make a point-source injection collisional model fit the observations for each of the events studied.
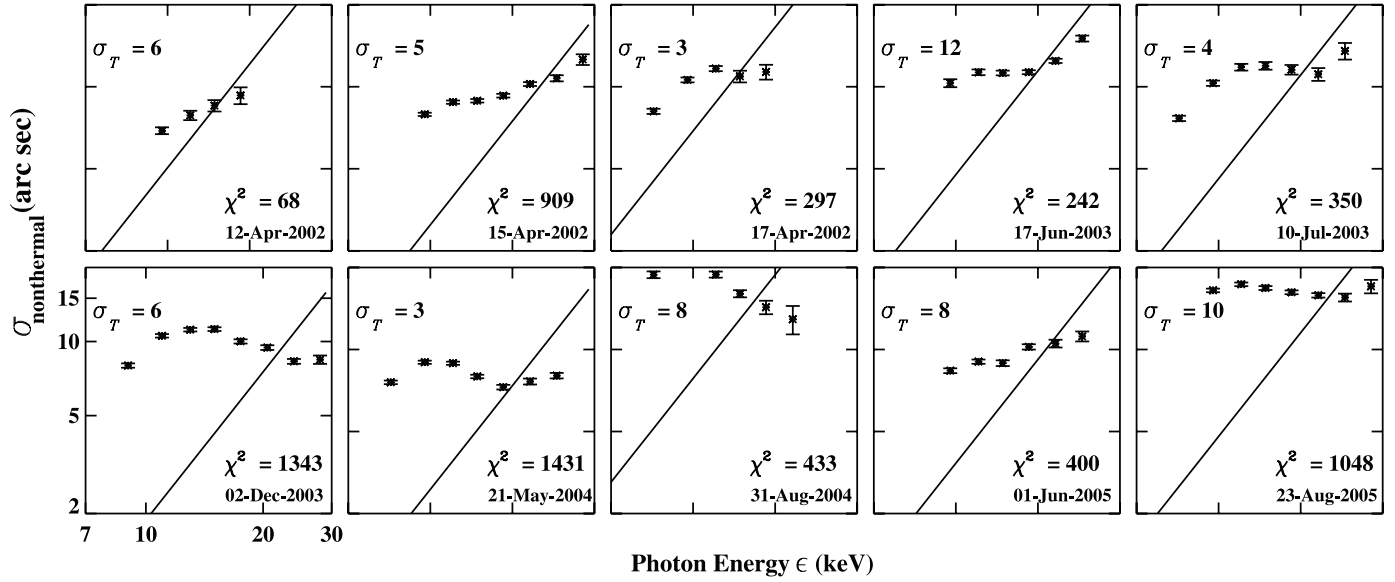
Fig. 7 panels (top two rows):

Row 1:
- $\sigma_T = 6$ | $\chi^2 = 68$ | 12-Apr-2002
- $\sigma_T = 5$ | $\chi^2 = 909$ | 15-Apr-2002
- $\sigma_T = 3$ | $\chi^2 = 297$ | 17-Apr-2002
- $\sigma_T = 12$ | $\chi^2 = 242$ | 17-Jun-2003
- $\sigma_T = 4$ | $\chi^2 = 350$ | 10-Jul-2003

Row 2:
- $\sigma_T = 6$ | $\chi^2 = 1343$ | 02-Dec-2003
- $\sigma_T = 3$ | $\chi^2 = 1431$ | 21-May-2004
- $\sigma_T = 8$ | $\chi^2 = 433$ | 31-Aug-2004
- $\sigma_T = 8$ | $\chi^2 = 400$ | 01-Jun-2005
- $\sigma_T = 10$ | $\chi^2 = 1048$ | 23-Aug-2005

y-axis: $\sigma_{\mathrm{nonthermal}}$ (arc sec); x-axis: **Photon Energy** ϵ **(keV)**

FIG. 7.—Point-source injection model fits to the "nonthermal" source sizes $\sigma_{\mathrm{nonth}}(\epsilon)$ (eq. [22]). The best-fit value for σ_T, the width of the Gaussian temperature distribution (eq. [3]) of the deconvolved thermal component, is shown, as well as the reduced χ^2 for the resulting fit to the nonthermal component.

Fig. 8 panels (four rows):

Row 1:
- $L = 3.62 \pm 0.29$; $n_{11} = 2.31 \pm 0.42$; $\chi^2 = 0.18$ | 12-Apr-2002
- $L = 4.72 \pm 0.06$; $n_{11} = 2.66 \pm 0.08$; $\chi^2 = 3.56$ | 15-Apr-2002
- $L = 4.07 \pm 0.15$; $n_{11} = 3.29 \pm 0.49$; $\chi^2 = 4.52$ | 17-Apr-2002
- $L = 7.55 \pm 0.22$; $n_{11} = 2.50 \pm 0.18$; $\chi^2 = 5.92$ | 17-Jun-2003
- $L = 4.97 \pm 0.11$; $n_{11} = 3.77 \pm 0.41$; $\chi^2 = 8.63$ | 10-Jul-2003

Row 2:
- $L = 6.83 \pm 0.05$; $n_{11} = 15.82 \pm 2.09$; $\chi^2 = 36.48$ | 02-Dec-2003
- $L = 2.99 \pm 0.02$; $n_{11} = 4.83 \pm 0.15$; $\chi^2 = 58.42$ | 21-May-2004
- $L = 5.39 \pm 0.17$; $n_{11} = 1.76 \pm 0.16$; $\chi^2 = 2.77$ | 31-Aug-2004
- $L = 5.45 \pm 0.14$; $n_{11} = 2.37 \pm 0.16$; $\chi^2 = 4.11$ | 01-Jun-2005
- $L = 8.72 \pm 0.08$; $n_{11} = 3.00 \pm 0.15$; $\chi^2 = 18.09$ | 23-Aug-2005

Row 3:
- $L = 1.38 \pm 0.49$; $n_{11} = 0.74 \pm 0.09$; $\sigma_T = 8.5$; $\chi^2 = 3.6$ | 12-Apr-2002
- $L = 6.25 \pm 0.12$; $n_{11} = 2.63 \pm 0.16$; $\sigma_T = 7.0$; $\chi^2 = 3.6$ | 15-Apr-2002
- $L = 5.71 \pm 0.31$; $n_{11} = 0.43 \pm 0.04$; $\sigma_T = 4.1$; $\chi^2 = 19.9$ | 17-Apr-2002
- $L = 7.87 \pm 0.28$; $n_{11} = 1.89 \pm 0.17$; $\sigma_T = 15.8$; $\chi^2 = 4.3$ | 17-Jun-2003
- $L = 6.42 \pm 0.21$; $n_{11} = 0.72 \pm 0.06$; $\sigma_T = 5.4$; $\chi^2 = 22.8$ | 10-Jul-2003

Row 4:
- $L = 8.84 \pm 0.12$; $n_{11} = 79.58 \pm 86.67$; $\sigma_T = 8.1$; $\chi^2 = 71.0$ | 02-Dec-2003
- $L = 6.82 \pm 0.10$; $n_{11} = 73.79 \pm 50.40$; $\sigma_T = 3.8$; $\chi^2 = 38.4$ | 21-May-2004
- $L = 13.63 \pm 0.64$; $n_{11} = 6.66 \pm 3.74$; $\sigma_T = 10.9$; $\chi^2 = 43.5$ | 31-Aug-2004
- $L = 6.19 \pm 0.20$; $n_{11} = 9.67 \pm 0.91$; $\sigma_T = 11.0$; $\chi^2 = 4.0$ | 01-Jun-2005
- $L = 14.35 \pm 0.27$; $n_{11} = 12.17 \pm 4.91$; $\sigma_T = 13.7$; $\chi^2 = 4.1$ | 23-Aug-2005

y-axis (rows 1–2): σ (arc sec); y-axis (rows 3–4): $\sigma_{\mathrm{nonthermal}}$ (arc sec); x-axis: **Photon Energy** ϵ **(keV)**
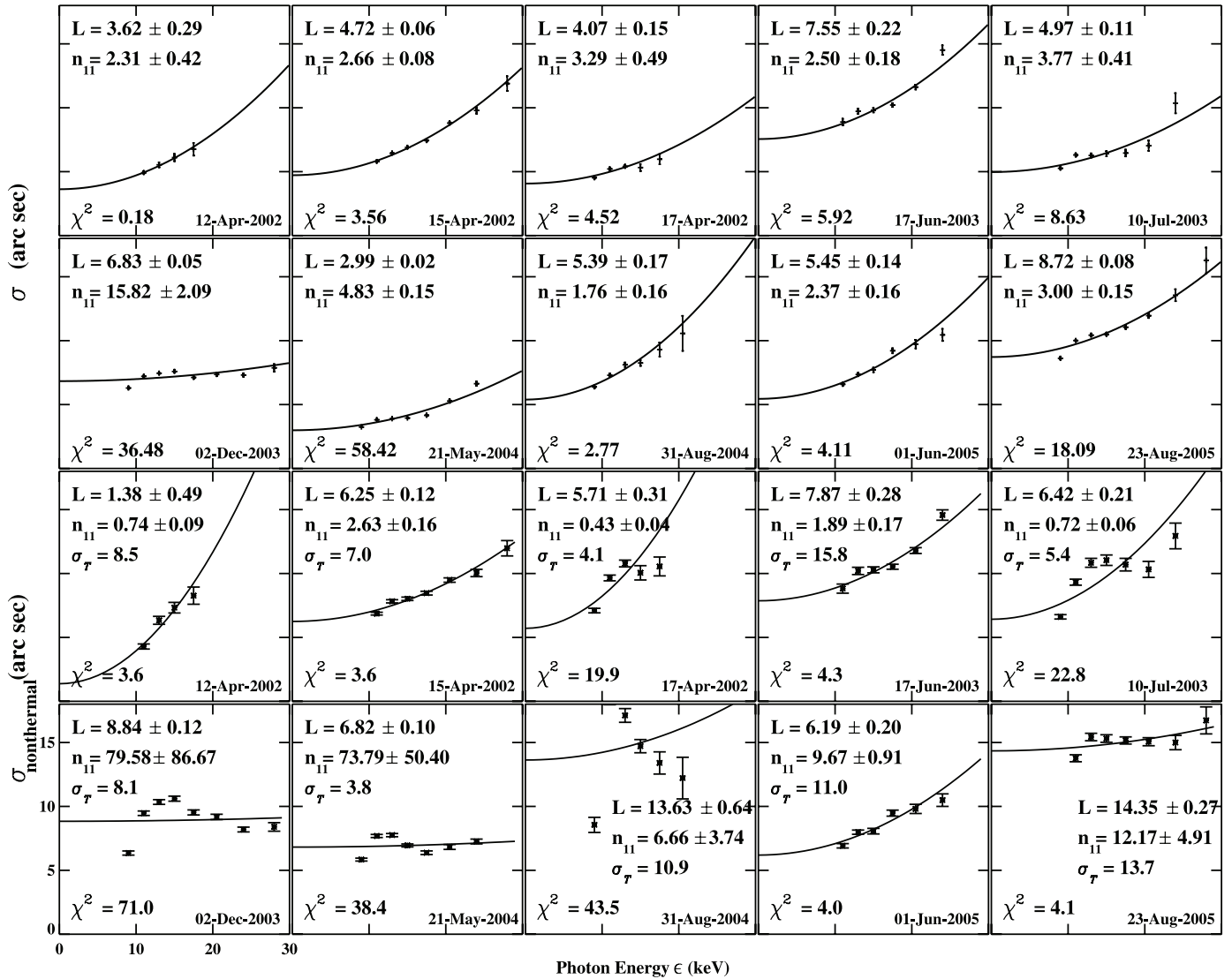
FIG. 8.— "Tenuous" acceleration region model (eq. [18]) fits to (*first and second rows*) the source sizes $\sigma(\epsilon)$. L is the half-length of the acceleration region (arcseconds), and n_{11} is the acceleration region density in units of 10^{11} cm^{-3}. *Third and fourth rows:* Fits to the deconvolved "nonthermal" source sizes $\sigma_{\mathrm{nonth}}(\epsilon)$ (eq. [22]). Here σ_T is the width (arcseconds) of the thermal distribution (eq. [3]) used in deconvolving the thermal component.
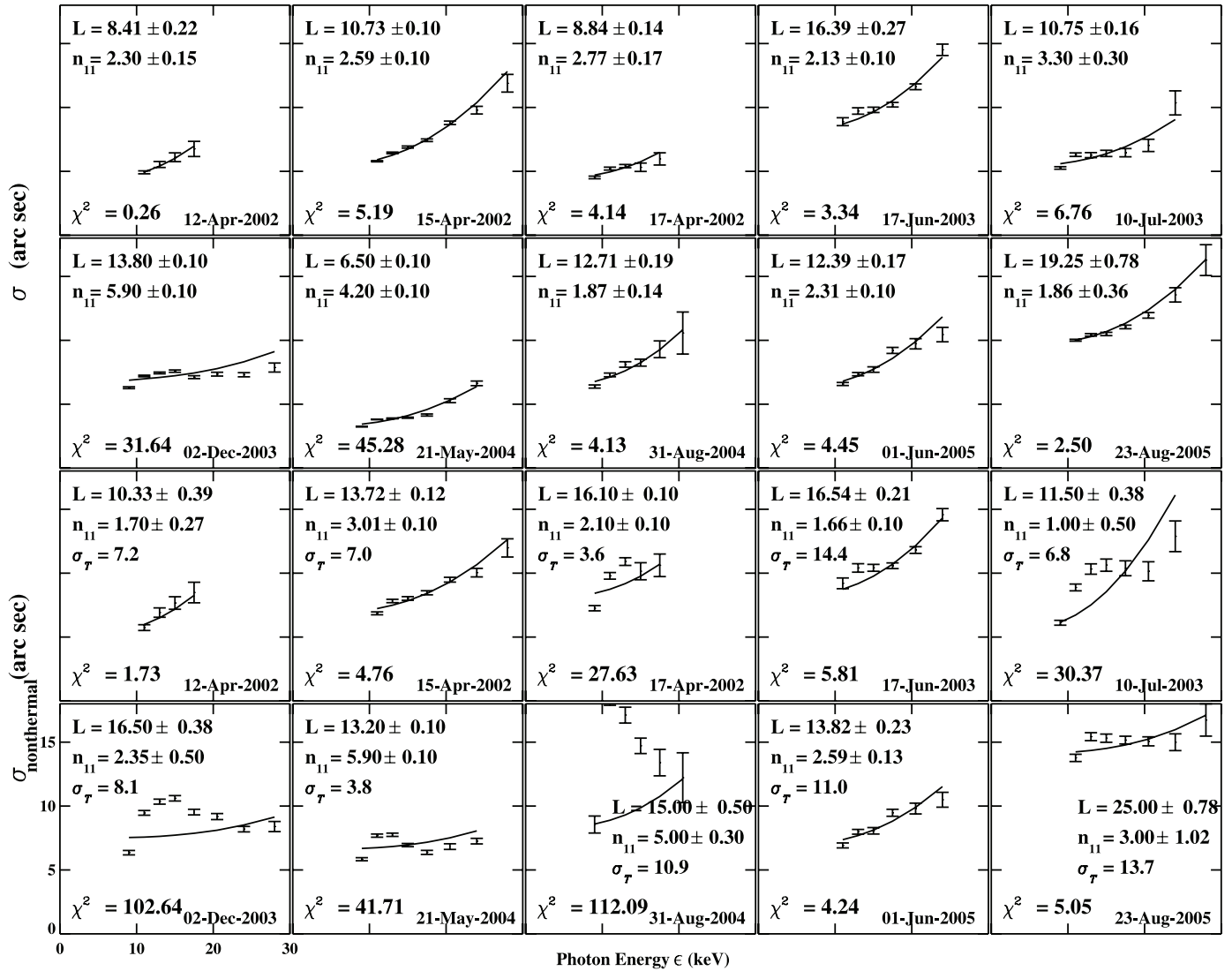
FIG. 9.—Same as Fig. 8, but for the "dense" acceleration region model (eq. [20]).

point-source injection collisional nonthermal models are shown in Figure 7. The obvious poor fit (and the reduced χ^2 values of the order of a few hundred!) show convincingly that such a "hybrid" model cannot account for the observed behavior of source size with photon energy. Furthermore, it would be expected that such a hybrid model would exhibit widespread (thermal) emission at low energies, the appearance of a compact thermal kernel (plus possibly the onset of nonthermal emission) at medium energies, and extended nonthermal emission at high energies. Such a behavior is completely inconsistent with the observed gradual increase in σ with ϵ. We therefore conclude that *the observed behavior of $\sigma(\epsilon)$ is consistent neither with a thermal model, nor with a point-source injection nonthermal model, nor with a combination of the two.*

We are therefore driven to a consideration of models that invoke an extended acceleration region (§§ 4.2.4 and 4.2.5). The first two rows of Figure 8 show that a quite acceptable fit to the values of $\sigma(\epsilon)$ is obtained with the form $\sigma = L + bn^{-1}\epsilon^2$, corresponding to the model that includes a (tenuous) acceleration region of finite length L. This suggests that the (quite reasonable) inclusion of an acceleration region of finite length readily accounts for the observed behavior $\sigma(\epsilon)$. The bottom two rows of Figure 8 show the fit to the values of $\sigma_{\text{nonth}}(\epsilon)$ (eq. [22]), with the

optimum value of the thermal source parameter σ_T shown in each case. Many of the fits are significantly improved compared to those corresponding to a "pure" nonthermal model.

The values of the reduced χ^2 for some of the fits are quite large, which we believe is a consequence of the very rigid description of the model (e.g., uniform density distribution), which is unlikely to be precisely followed in the real world. However, the quality of the overall fits to the data (compared to the fit using a point-source injection model, whether or not in combination with a thermal source) indicates that a model with the general property of an extended acceleration region is a much better reflection of the true situation.

In Figure 9 we fit both $\sigma(\epsilon)$ (*top two rows*) and $\sigma_{\text{nonth}}(\epsilon)$ (*bottom two rows*) using the dense acceleration region model. Similar to the results for the tenuous–acceleration region model, both the "pure" nonthermal model and the corresponding "hybrid" model result in fits to the data that are considerably better than models that invoke a point-source acceleration region.

The values of χ^2 for the dense–acceleration region model, either alone or in combination with a thermal component, do not systematically differ from those for the tenuous–acceleration region model; consequently, the fits alone offer no basis to favor the dense-acceleration over the tenuous-acceleration model.
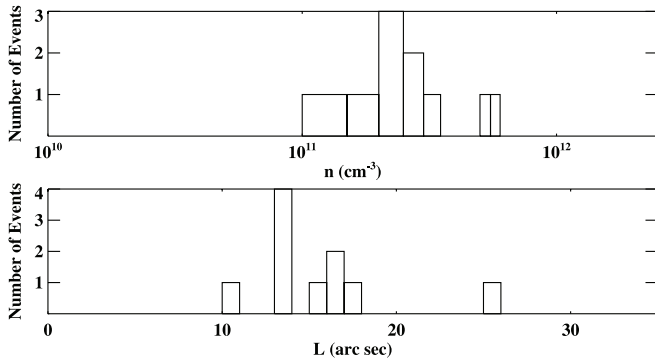
Fig. 10.—Values of source densities n and lengths L for all 10 events studied, for the "dense" extended-length acceleration region model.

However, the physical necessity for a nonempty acceleration region, plus the evident single-source (rather than double-source) X-ray morphology for these events, argues strongly in favor of the dense-acceleration model. Figure 10 shows histograms of n and L for the dense–acceleration region model for the 10 events studied. The acceleration region density lies in the range $(1-5) \times 10^{11}$ cm^{-3}, and its half-length L lies in the range $\sim 10''-18''$ (Fig. 10).

In summary, consideration of (1) a finite extent of the acceleration region for the nonthermal electrons and/or (2) the combination of thermal and nonthermal emission provides a natural explanation for the observed behavior of $\sigma(\epsilon)$; neither a hitherto unproposed electron energy loss process nor an implausible density profile in the bremsstrahlung source is required.

6. SUMMARY AND DISCUSSION

We have analyzed hard X-ray observations of limb flares with a relatively simple extended-source morphology at different photon energies. In a simple thermal model in which the temperature falls off with distance from the center of the source, the highest energy sources should be most localized near the temperature maximum and so the source size should *decrease* with photon energy. Consequently the generally observed *increase* in source size with photon energy (Fig. 1) argues persuasively *against* a thermal origin for solar hard X-ray emission in flares of this type. Note that this conclusion is independent of the form of the spatially integrated spectra for the events in question.

Furthermore, the quantitative behavior of $\sigma(\epsilon)$ also differs markedly from the prediction ($\zeta \equiv d \ln \sigma / d \ln \epsilon = 2$) of models in which electrons are injected from a compact acceleration region into a uniform-density loop and lose energy through Coulomb collisions. Although, as discussed in § 4.2.3, the point-source injection collisional model can be "rescued" by adopting a non-uniform density $n(s)$ in the region of electron propagation, the required density profiles (Fig. 6) all show variations in $n(s)$ that are unlikely to be present in the hydrodynamically relaxed state appropriate to the duration of the observation intervals used. The observed best-fit value $\zeta \simeq \frac{1}{2}$ is also inconsistent with all non-collisional energy loss processes hitherto proposed.

Looptop acceleration models (Shibata et al. 1995; Tsuneta 1997; Shibata 1998; Masuda et al. 2000) are well approximated by a point-source injection model. Hence, although such models have otherwise proved quite successful in accounting for observations (e.g., Masuda 1994), they would appear to be effectively ruled out as viable models for the extended-source events studied here. On the other hand, as shown in Figure 9, the nonthermal collisional model *can* be rather straightforwardly brought into agreement with the observations *by adopting a finite length for the acceleration region* and endowing it with the same density as the rest of the loop.

Our results also permit the determination of both the length and density of the acceleration region. For most events, the acceleration region density lies in the range $(1-5) \times 10^{11}$ cm^{-3} and its half-length L lies in the range $\sim 10''-18''$ (Fig. 10). These are significant constraints, and, to our knowledge, they represent the first *empirical* quantitative estimates of the physical characteristics of electron acceleration regions in solar flares.

REFERENCES

Brown, J. C., Aschwanden, M. J., & Kontar, E. P. 2002, Sol. Phys., 210, 373
Emslie, A. G. 1980, ApJ, 235, 1055
Emslie, A. G., Barrett, R. K., & Brown, J. C. 2001, ApJ, 557, 921
Emslie, A. G., & Smith, D. F. 1984, ApJ, 279, 882
Forbes, T. G., & Malherbe, J. M. 1986, ApJ, 302, L67
Haydock, E. L., Brown, J. C., Conway, A. J., & Emslie, A. G. 2001, Sol. Phys., 203, 355
Hirayama, T. 1974, Sol. Phys., 34, 323
Holman, G. D., Sui, L., Schwartz, R. A., & Emslie, A. G. 2003, ApJ, 595, L97
Hurford, G. J., et al. 2002, Sol. Phys., 210, 61
Kopp, R. A., & Pneuman, G. W. 1976, Sol. Phys., 50, 85
Lin, J., & Forbes, T. G. 2000, J. Geophys. Res., 105, 2375
Lin, R. P., et al. 2002, Sol. Phys., 210, 3

Mariska, J. T., Emslie, A. G., & Li, P. 1989, ApJ, 341, 1067
Masuda, S. 1994, Ph.D. thesis, Univ. Tokyo
Masuda, S., Sato, J., Kosugi, T., & Sakao, T. 2000, Adv. Space Res., 26, 493
Shibata, K. 1998, Ap&SS, 264, 129
Shibata, K., Masuda, S., Shimojo, M., Hara, H., Yokoyama, T., Tsuneta, S., Kosugi, T., & Ogawara, Y. 1995, ApJ, 451, L83
Smith, D. M., et al. 2002, Sol. Phys., 210, 33
Somov, B. V., & Kosugi, T. 1997, ApJ, 485, 859
Tandberg-Hanssen, E., & Emslie, A. G. 1988, The Physics of Solar Flares (Cambridge: Cambridge Univ. Press)
Tsuneta, S. 1997, ApJ, 483, 507
Veronig, A. M., & Brown, J. C. 2004, ApJ, 603, L117